Solar-Terrestrial Physics. 2026, vol. 12, iss. 2, pp. 8–20. DOI: 10.12737/stp-122202602. © 2026 V.V. Grechnev, M.V. Globa, A.M. Uralov Published by INFRA-M Academic Publishing House

DOI: 10.12737/stp-122202602
EDN: GCEIUR

Received November 16, 2025
Accepted January 15, 2026

ERUPTION OF A HIGH-LATITUDE PROMINENCE OBSERVED BY THE SIBERIAN RADIOHELIOGRAPH AND SPACE-BORNE TELESCOPES: I. TORUS AND HELICAL KINK INSTABILITIES IN CME DEVELOPMENT

V.V. Grechnev
Institute of Solar-Terrestrial Physics SB RAS, Irkutsk, Russia, grechnev@iszf.irk.ru

M.V. Globa
Institute of Solar-Terrestrial Physics SB RAS, Irkutsk, Russia, globa@iszf.irk.ru

A.M. Uralov
Institute of Solar-Terrestrial Physics SB RAS, Irkutsk, Russia, uralov@iszf.irk.ru

Abstract. The eruption of a large prominence and the resulting development of a coronal mass ejection (CME) were observed on June 12, 2023 by the Siberian Radioheliograph in microwaves up to heliocentric distances exceeding two solar radii, space-borne telescopes in the extreme ultraviolet, and coronagraphs in white light. The evolution of the CME structural components was traced and their kinematic characteristics were measured. The CME components underwent two successive acceleration pulses, comparable in magnitude and duration. According to the observations, the first acceleration pulse was caused by torus instability of the magnetic flux rope associated with the prominence. At this stage, its expansion was self-similar and consistent with the expansion of the CME frontal structure. The frontal structure was an expanding arcade that encompassed the pre-eruption prominence. The second acceleration pulse was associated with helical kink instability, which manifested itself in the deformation of the top of the erupting prominence, visible as a helical protrusion. The development of helical kink instability affected the motion of the CME frontal structure, but did not influence the motion of the main body of the CME core, shown up as the massive part of the erupting prominence beneath the helical protrusion. After the completion of the helical kink instability, the coordinated self-similar expansion of all CME components recovered. The fact that the helical kink instability occurred much later than the torus instability excludes its involvement in causing the latter, as has sometimes been assumed.

Keywords: Sun, eruptive prominence, CME, Siberian Radioheliograph, kinematic characteristics, magnetic flux rope, torus and helical kink instabilities.

INTRODUCTION

Solar eruptions, i.e. ejections of magnetized plasma, are the initial stages of the formation of coronal mass ejections (CMEs) and can be accompanied by flares, shock waves, and energetic particle fluxes. All these phenomena are potential sources of space weather disturbances that threaten the operation of various space-borne and ground-based systems. While there is a sharp difference in the manifestations between events associated with powerful flares and those related to eruptions of large prominences away from active regions, the processes responsible for them are probably the same, and the differences are purely quantitative [Švestka, 2001]. Non-flare-associated eruptions can lead to significant space-weather disturbances too. In such cases, an important factor is also the size of the event. For example, the eruption of a large prominence on September 29, 2013 resulted in a Forbush decrease, a geomagnetic storm, and a large near-Earth proton enhancement with proton energies exceeding 100 MeV [Bruno et al., 2018; Grechnev, Kuzmenko, 2020]. These circumstances determine the practical significance of non-flare-associated eruptions for space weather.

Such events also appear promising for studying the development of eruptions and the formation of CMEs. The absence of bright flare emission in such events facilitates the observation of eruptive prominences. The large size of such prominences promotes the identification of their structure. The long duration of their lift-off simplifies measurements of their kinematic characteristics. These features of non-flare-associated eruptions of large prominences favor observational studies of driving factors of eruptive processes and further development of CMEs.

The magnetic structure of a solar prominence (filament) before eruption is usually approximately represented as a magnetic flux rope. Two main magnetohydrodynamic (MHD) instabilities, torus and helical kink, may be responsible for the eruption and changes in the shape of the magnetic flux rope. The role and conditions of development of each of these instabilities differ. According to model studies of magnetic flux ropes (e.g., [Amari et al., 2000, 2014; Aulanier et al., 2010]), the most probable driving factor of an eruption is torus instability [Shafranov, 1966; Bateman, 1978; Chen, 1989;

Kliem, Török, 2006; Schmieder et al., 2013]. A simplified analog of such instability is the instability of a rectilinear unscreened current above the photosphere (e.g., [van Tend, Kuperus, 1978; Molodenskii, Filippov, 1987]). To trigger torus instability, in addition to sufficient magnetic twist, the flux rope must rise and reach the zone of rapid decay of the external transverse magnetic field, which prevents expansion. This occurs during the initiation stage, when, due to acts of magnetic reconnection (e.g., tether cutting [Moore et al., 2001]), a magnetic flux rope is formed and slowly rises into the instability zone. After that, unlimited toroidal expansion of the prominence becomes possible.

The development of the helical kink instability requires only sufficient twist of the flux rope exceeding a certain critical value. In the case of a force-free magnetic field $\nabla\times\mathbf{B}=\alpha\mathbf{B}$, it is also necessary to violate the condition $\nabla\alpha=0$. Unlike the torus instability, the helical kink instability [Shafranov, 1970; Kadomtsev, 1966; Bellan, 2008] is not able to provide unlimited eruption of a magnetic flux rope, but it can destroy or change the entire magnetic configuration [Amari, Luciani, 1999; Hassanin, Kliem, 2016; Hassanin et al., 2022].

Observations of erupting structures over a wide range of heights, changes in their shape, and measurements of their motions can contribute to the study of solar eruptions, the development of CMEs, and the elucidation of the role of MHD instabilities. Common problems with such measurements are a rapid decrease in brightness or opacity of erupting structures during their expansion and the impulsive nature of acceleration. In flare-associated events, the main acceleration occurs in the impulsive phase before an erupting structure appears in the field of view of a coronagraph. During eruptions of large prominences unrelated to obvious flare manifestations, the acceleration is considerably lower in magnitude and continues longer than during flare-associated eruptions. Along with the initial main acceleration pulse, in such events additional comparable acceleration is sometimes recorded at a considerable distance from the Sun (e.g., [Kuzmenko, Grechnev, 2017; Grechnev, Kuzmenko, 2020]). Difficulties in identifying the structures observed by coronagraphs with those visible in the extreme ultraviolet near the solar surface also prevent complete measurements of their motions and the detection of ongoing changes.

At present, prominences can be studied using almost continuous observations in the extreme ultraviolet (EUV) range, especially in the HeII 304 Å line. Microwave images can significantly complement these observations. They can be employed to measure motions of erupting prominences and estimate plasma parameters in them [Gopalswamy, Hanaoka, 1998; Grechnev et al., 2006; Shimojo et al., 2006; Uralov et al., 2023]. Under favorable conditions, radioheliographs' fields of view can overlap with coronagraphs's fields of view.

This study analyzes the eruption of a large high-latitude prominence and the development of CME observed by space-borne telescopes and the Siberian Radioheliograph (SRH) [Altyntsev et al., 2020] in different emission ranges. This article, Article I, examines the structure, kinematic characteristics, and shape changes of the eruptive prominence and CME. Article II deals with microwave observations of plasma streams falling from the erupting prominence onto the solar surface.

Section 1 of this article provides a general overview of the event, discusses data handling techniques, and analyzes observations. Section 2 discusses the results. The final section summarizes the findings of the study.

1. EVENT OVERVIEW, OBSERVATIONS, AND DATA HANDLING

1.1. Initial stage of eruption

On June 12, 2023 at 02:00–03:30 UTC (hereinafter Coordinated Universal Time is used), a large prominence, located approximately along the parallel at latitudes N62–N70, erupted. The eruption was observed by SRH at a number of frequencies. In EUV, prominences, including eruptive ones, are best seen in the HeII 304 Å line with a characteristic temperature of 50000 K. The eruption in question was observed in different channels, including 304 Å, by the Atmospheric Imaging Assembly (AIA) [Lemen et al., 2012] on board the Solar Dynamics Observatory (SDO) [Pesnell et al., 2012]. The event was also recorded by the Sun Earth Connection Coronal and Heliospheric Investigation (SECCHI) instrument suite [Howard et al., 2008] on board the Solar-Terrestrial Relations Observatory (STEREO) [Kaiser et al., 2008]. The advantage of the Extreme Ultraviolet Imager (EUVI) [Wuelser et al., 2004] on STEREO-A is its wider field of view compared to SDO/AIA.

This study uses SRH observations made at a frequency of 6.2 GHz at which the eruptive prominence is best visible. From SRH data, we synthesized image sets for the stage of slow rise of the prominence from 00:15 to 02:00 with a typical interval of 352 s (5.87 min) and then from 02:00 to 04:30, when the prominence rise sped up, with a typical interval of 70.5 s (1.18 min). The half-height cross-section of the 6.2 GHz SRH beam pattern had the shape of an ellipse with axes 18″×27″ at 02:00 and was almost circular, 22″×22″, at 03:33.

In this study, the SRH images were calibrated in brightness temperatures, using the following well-known approach. Due to the statistical predominance in the image of pixel values corresponding to the levels of the sky and the quiet Sun at a given frequency, the brightness distribution histogram has two peaks. For example, by referring instrumental units to the histogram peaks, Nobeyama Radioheliograph data was calibrated [Hanaoka et al., 1994]. Difficulties, however, arise when the histogram peaks are distorted or there are very bright sources. The biggest problems occur when the two histogram peaks are not separated.

To overcome such difficulties, this technique has been updated [Kochanov et al., 2013]. Brightness distributions within the solar disk and over the sky region outside it are analyzed separately. To reduce the influence of spurious spikes and other histogram problems, the result of its fit with a Gaussian is used. The quiet Sun's brightness temperature at the required frequency is calculated by a procedure that fits the measurements

presented in [Zirin et al., 1991; Borovik, 1994]. At a frequency of 6.2 GHz, quiet Sun's brightness temperature is taken to be 15810 K.

Figure 1 displays images of the eruptive prominence during its slow rise, which were obtained with SDO/AIA in the 193 Å and 304 Å channels and with SRH at 6.2 GHz. The images in the top row are presented on a logarithmic scale; for better visibility, the brightness is limited from above at 50 % of the maximum. The same images in the bottom row have enhanced contrast. For the image in Figure 1, *d* (AIA 193 Å), the threshold is lowered to 10 % and a power-law function with an exponent of 0.5 is used for the image presentation. The AIA 304 Å image in Figure 1, *e* is divided by a radial brightness distribution and the result is limited by thresholds 0.1 and 2.0. The radial brightness distribution is subtracted from the SRH image in Figure 1, *f*, and the difference is limited by ±8000 K thresholds (±1.3 % of the maximum). The radial brightness distributions are depicted in Figure 2.

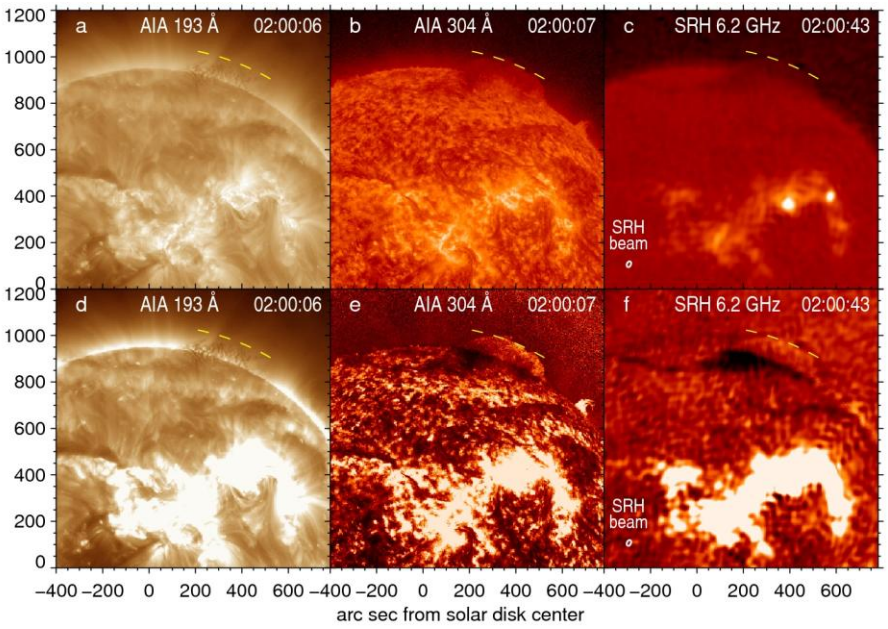

Figure 1. High-latitude prominence during its slow rise, observed by SDO/AIA in 193 Å (*a*, *d*) and 304 Å (*b*, *e*) and by SRH at 6.2 GHz (*c*, *f*): top row — log-scale images with moderate brightness thresholding; bottom row — the same images with enhanced contrast. The AIA 304 Å (*e*) and SRH (*f*) images are corrected for radial brightness distributions (division is used in panel *e*; subtraction, in panel *f*) and are limited by brightness above and below. The upper edge of the prominence is outlined by the yellow dashed arc. The small white ellipse in panels *c* and *f* is the cross-section of the SRH beam pattern at half-height level

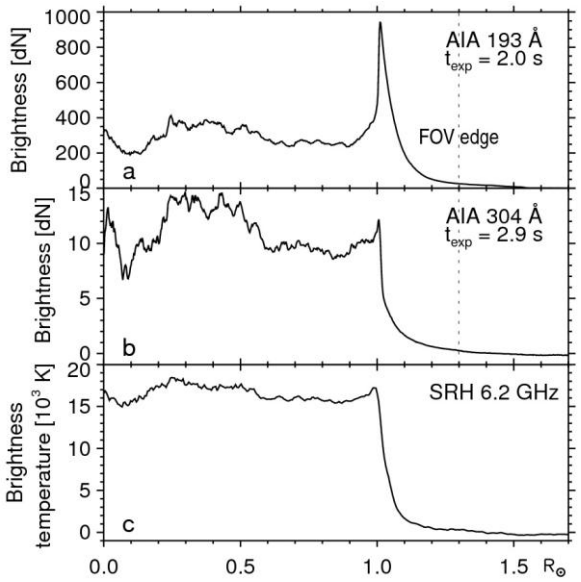

Figure 2. Radial brightness distributions in SDO/AIA images in 193 Å (*a*) and 304 Å (*b*) and in SRH images at 6.2 GHz (*c*). Exposure durations are 2.0 s for AIA 193 Å and 2.9 s for AIA 304 Å images. The vertical dotted line in panels *a* and *b* indicates the edge of the AIA field of view in the northern direction

Dividing by the radial brightness distribution produces a result somewhat similar to using a radial filter. The advantages of this method over dividing by an image before the event are the absence of the solar rotation effect and lower noise in the array on which the division is made, compared to a single image. The disadvantage is that it ignores the inhomogeneities of the corona depending on the azimuth (position angle), which is insignificant in our case when only the directions that include the eruptive prominence are of interest. Dividing by the radial brightness distribution is effective for EUV images, which have high sensitivity and low noise. For microwave images, which have higher noise and uneven background, subtracting the radial distribution or its fraction is more effective. This processing results in increased contrast of the prominence.

The prominence structure in the AIA 193 Å images (see Figure 1, *a* and *d*) is highly inhomogeneous and contains dark helical threads screening the bright corona behind them. Consequently, these threads absorbed the coronal emission, which indicates their low temperature. A small coronal hole is visible in the lower-left corner of the images, just east of the disk center. The AIA 304 Å images (Figure 1, *b* and *e*)

also reveal an inhomogeneous threadlike structure of the prominence.

Figure 1, *c* and *f* presents an SRH image. Figure 1, *f* demonstrates the prominence's eastward extension, as well as a dark filament southwest of the eruptive prominence. This filament is also visible in the AIA 193 Å and 304 Å images. The bright regions in all three images are similar too.

As the AIA 304 Å and SRH images in panels *d*, *e*, and *f* show, dividing by the radial brightness distribution or subtracting it enhances contrast of the eruptive prominence against both the solar disk and the sky. This emphasizes the prominence body and leading edge, facilitating more accurate measurements of its position and brightness temperature. In the SRH image shown in Figure 1, the average brightness temperature of the prominence against the solar disk is 9130±1400 K (at level 1σ); against the sky, 3450±800 K. Sky background fluctuations at level 1σ are ≈1000 K. The maximum brightness temperature in this SRH image is as high as 0.6 MK (minimum –13400 K). Brightness temperatures in SRH images at different frequencies are discussed in Article II.

Further, when examining EUV and microwave observations, we use partial or full correction of the images for the radial brightness distribution. These distributions, shown in Figure 2, were obtained by circular scanning of the images. Each radius value corresponds to the most probable brightness value along the circumference of this radius.

Shapes of the radial distributions in different emission ranges are similar, as expected given the general similarity between the images in Figure 1, but the relationships between their parts are not identical. In the 193 Å channel, there is a strong limb brightening typical of the optically thin corona. The limb brightening is observed in the EUV channels dominated by iron emission lines (171–175 Å, 193–195 Å, 211 and 284 Å, etc.) and is expected at high radio frequencies [Zheleznyakov, 1970]. In the radial radio brightness distribution in the SRH image (see Figure 2, *c*), the limb peak is weakly pronounced. This may be due to factors related to the optical thickness of the corona at 6.2 GHz, as well as insufficient resolution and other instrumental limitations of SRH.

The vertical dotted line in Figure 2, *a* and *b* indicates the northern edge of the SDO/AIA field of view. SRH has a much wider field of view. It is limited by the presence of solar images from adjacent interference maxima in the direction of interest, as well as by SRH sensitivity. In Figure 2, *c*, the radio brightness distribution is given only out to the heliocentric distance of $1.7R_{\odot}$ to better demonstrate the distribution across the solar disk; at larger distances, the radio brightness is almost constant. In this event, the top of the erupting prominence is detectable in SRH images at 6.2 GHz out to a heliocentric distance of $2.2R_{\odot}$.

1.2. Kinematics of the erupting prominence according to SRH observations

Figure 3 exhibits four episodes of prominence eruption observed by SRH. The prominence top is visible clearly enough to measure the position of its leading edge. Initially, the top rose mostly in one direction between two dotted lines, each at an angle of –15° to the Sun's polar axis. Then, the eastern (left in Figure 3) edge of the prominence began to stretch forward, which is confirmed by subsequent coronagraph images. The distance between the inclined dotted lines was chosen to ensure that the prominence top remained between them.

There are two approaches to measuring speeds and accelerations of erupting structures. One approach uses differentiation of time-distance measurements to obtain speeds. The scatter of results is usually large because of observational difficulties in identifying the position of the leading edge of the erupting structure. This scatter complicates the second differentiation for estimating acceleration. To overcome this difficulty, spline smoothing [Vršnak et al., 2007] and a more sophisticated method using regularization [Temmer et al., 2010] have been proposed. In addition to the above works, this approach was adopted, for example, in [Bein et al., 2011; Berkebile-Stoiser et al., 2012].

Note that with the achievable measurement accuracy no method can identify the shape of the acceleration pulse due to the double integration required to transit from the desired acceleration to measurable time-distance points. It is only possible to estimate the acceleration pulse area (i.e., the speed difference) and its centroid time and effective duration.

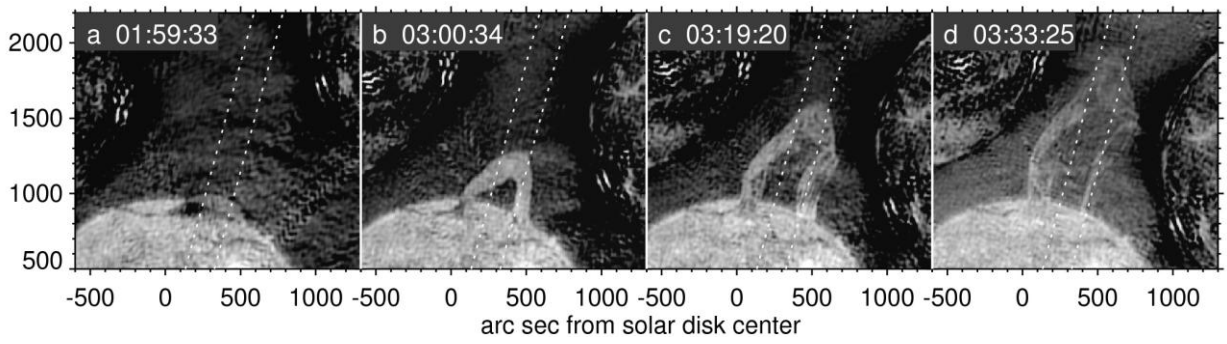

Figure 3. Episodes of prominence eruption observed by SRH at 6.2 GHz. In all images, 60 % of the radial brightness distribution has been subtracted, and a nonlinear scale has been used. The dotted lines at –15 ° to the north correspond to the main motion of the prominence top. Averaging in the band between the dashed lines was made to compute the one-dimensional profile presented in Figure 4

Another approach involves fitting the observed motion of the erupting structure by an analytical function [Gallagher et al., 2003; Sheeley et al., 2007; Wang et al., 2009; Alissandrakis et al., 2013]. In the simplest case, the eruptive structure starts to move with a low speed and after an impulsive acceleration acquires a high constant final speed. The corresponding speed evolution is close in shape to a hyperbolic tangent or error function. Assuming that the acceleration pulse has, for example, the Gaussian shape, we can estimate its area from the difference between the final and initial speeds, find the time of the maximum by comparing the result of its double integration with the measured time–distance points, and adjust the duration according to the curvature of the acceleration segment. For instance, acceleration shaped as a δ-function corresponds to a break in the time–distance plot, whereas a longer acceleration is typical of a smoother transition from the initial to final speed. In the case of more complex kinematics, a combination of two or more acceleration pulses is used (e.g., [Grechnev et al., 2016, 2022, 2024]).

To measure the motion of the eruptive prominence, a one-dimensional spatial profile is employed. Each its column is calculated as the average across a relatively narrow strip of the given image along the direction of motion. This representation is similar to stack plots [Ma et al., 2011; Alissandrakis et al., 2013], but provides higher sensitivity. By adjusting the acceleration parameters, an acceptable match between the calculated time–distance curve and the trace of the erupting prominence on the one-dimensional profile is achieved.

Figure 4 displays the one-dimensional profile computed from all SRH images in the strip between the inclined dotted lines in Figure 3. The radial radio brightness distribution, shown in Figure 2, *c*, was subtracted from each SRH image. To emphasize the bright trace of the prominence, each column of the profile was normalized by its extreme values outside the solar disk. The kinematic plots corresponding to the dashed curve along the trace of the prominence are presented in Figure 5.

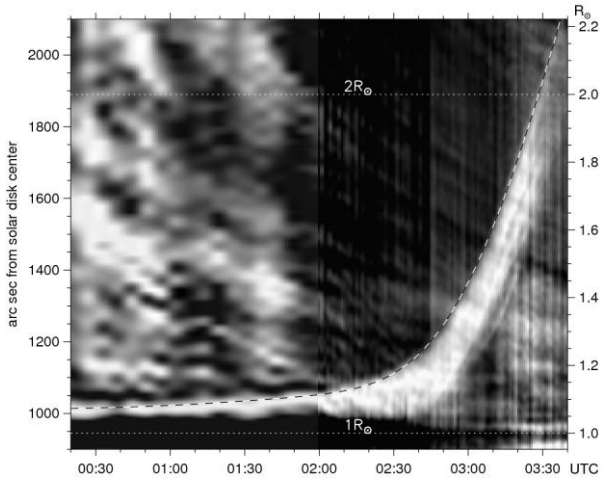

Figure 4. One-dimensional profile of eruptive prominence motion computed from all SRH images with the radial radio brightness distribution subtracted. Each column of the profile represents the average of one SRH image across the strip enclosed between the dotted lines in Figure 3. The dashed curve fits the rise of the prominence top. Horizontal dotted lines $1R_\odot$ and $2R_\odot$ denote the corresponding heliocentric distances

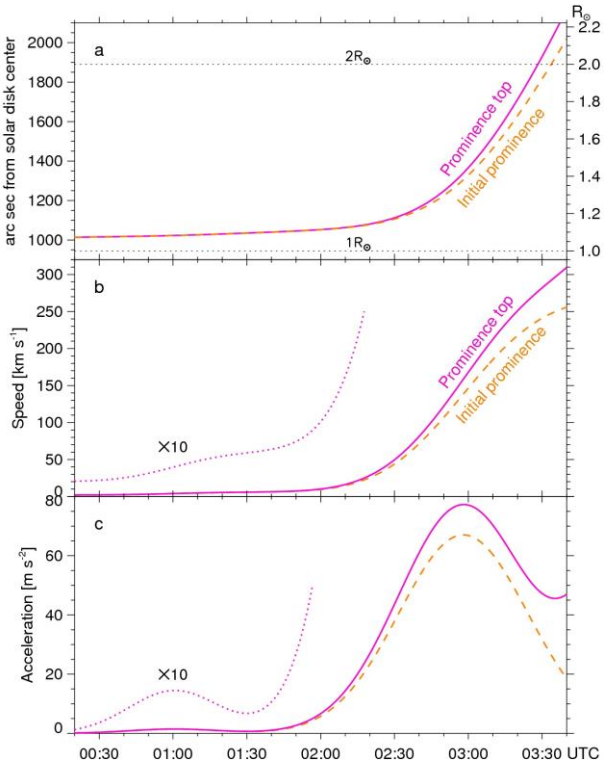

Figure 5. Kinematics of the leading edge of the erupting prominence according to SRH data: *a* — heliocentric distances of the eruptive prominence (orange dashed line) and its top (solid magenta line). Black dotted lines denote $1R_\odot$ and $2R_\odot$; *b*, *c* — speed and acceleration plots. The magenta dotted line indicates the initial part of the plot magnified by a factor of 10

The solid magenta curve in Figure 5, *a* is identical to the dashed curve outlining the prominence trace in Figure 4; and the magenta curves in Figure 5, *b* and *c* represent the corresponding speed and acceleration variations. A clear acceleration of the prominence, lasting approximately an hour at half-height, occurred around 02:58. Nonetheless, when using a single acceleration pulse, it is impossible to reproduce the entire trajectory of the prominence: its calculated rise begins earlier than the actual one. To be consistent with observations, an additional weak acceleration pulse is required around 01:00. At this time, the prominence began to rise noticeably, with its speed reaching 6 km/s. This slow rise of the prominence might have been related to the initiation stage.

On the other hand, for the dashed curve to match the prominence trace in the final part of the trajectory after 03:20 in Figure 4, another, later acceleration pulse is required. The SRH data represents the prominence lift-off out to the heliocentric distance of $2.2R_\odot$. Measuring its subsequent acceleration calls for wider-field observations discussed below.

1.3. General characterization of CME

In images obtained by the C2 Large Angle Spectroscopic Coronagraph (LASCO) [Brueckner et al., 1995] of the Solar and Heliospheric Observatory (SOHO) [Domingo et al., 1995], from 03:12 a CME was observed in the region of position angles close to the direc-

tion of motion of the eruptive prominence in Figure 3. The position angle is calculated counterclockwise from North. This CME, visible in Figure 6 slightly west of the North Pole, probably resulted from the eruptive event in question. In the online CME catalog [http://cdaw.gsfc.nasa.gov/CME_list/] [Yashiro et al., 2004] based on SOHO/LASCO observations, the speed of the fastest feature (FF) of this CME is estimated to be 750 km/s at a heliocentric distance of $2.5R_\odot$ and 670 km/s at $27R_\odot$, an average speed of 714 km/s, and an average acceleration of –4 m/s^2.

For measurements in the CME catalog, enhanced-contrast running-difference images are used which are formed by subtracting its predecessor from each current image (see Figure 6, *a*). This representation clearly reveals the outer edge of expanding CME, providing acceptable accuracy in measuring its motion. However, features that were bright in the subtracted image appear dark in the difference image, and vice versa; therefore, it is difficult to analyze the internal CME structure from such images.

Since the main subject of this study is the eruptive prominence that later became the core of the CME, the representation in Figure 6, *b* is more convenient. Here, the same image at 04:12, which is displayed in Figure 6, *a*, is divided by a background image, each pixel of which

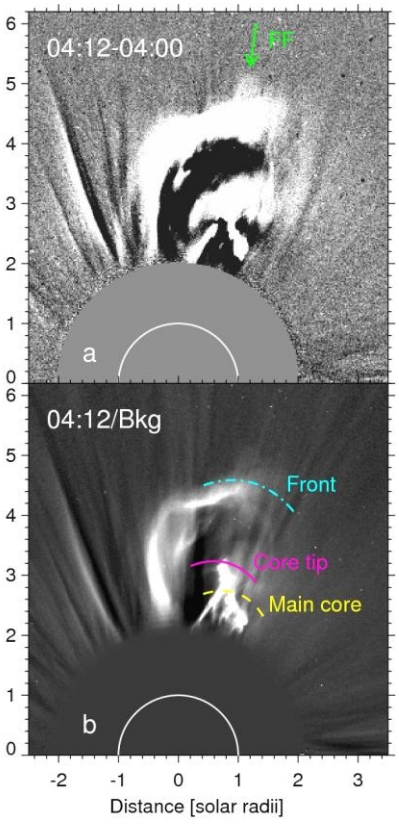

Figure 6. CME in SOHO/LASCO-C2 images. Panel *a*: enhanced-contrast difference with a preceding image — a representation close to that used in the CME catalog for measurements; the green arrow marks the fastest feature (FF). Panel *b*: the same image at 04:12 divided by the background image computed from several images obtained before the CME appearance; the CME structural components are outlined by colored arcs: the main core (yellow dashed), the core tip (solid magenta), and the frontal structure (dash-dotted cyan). The white arc is the solar limb

is calculated as the median value at the same pixel over five images from 02:00 to 02:28 before the CME appeared in the LASCO-C2 field of view. Next, a series of images are used for measurements, in which the leading edge of the measured structure is outlined by an arc, as in Figure 6, *b*. Arcs also trace the edges of prominent CME features: the main core, its tip, and the frontal structure. The time dependence of the radius of each arc is adjusted by varying the acceleration parameters until an acceptable match to the measured structure is achieved, as described in the previous section.

1.4. STEREO-A observations of the eruptive prominence

It is possible to follow the further expansion of the eruptive prominence before the CME appearance in the SOHO/LASCO-C2 field of view $(2–6.4)R_\odot$, using STEREO-A/SECCHI observations. During this event, STEREO-A was located 6.1° east of Earth and 5.8 % closer to the Sun. The latitude of the solar disk center viewed from STEREO-A was –0.07°; and viewed from SDO, about +0.6°. Thus, the structures expanding above the Sun were visible almost equally from Earth, SDO, and STEREO-A (corrected by 1.058), although there may be small differences. Figure 7 compares the images of the eruptive prominence obtained by SDO/AIA and STEREO-A/EUVI in the 304 Å channel, as well as by SRH. The yellow dashed arc corresponds to the middle of the prominence top; the solid magenta arc, to the forward-stretching eastern (left) part.

Further expansion of the eruptive prominence is traced in images obtained by STEREO-A/COR1 that has the $(1.4–3.6)R_\odot$ field of view. Figure 8 shows four COR1 images (top row) along with images obtained with SRH at close times (bottom row). In the damaged areas of the COR1 field of view, the eruptive prominence is not visible; however, in the selected images, its visible parts, including the top, correspond to each other in the images produced by both instruments. In Figure 8, *h*, the prominence is detectable almost at the SRH sensitivity limit; nevertheless, its eastern part is seen stretching forward.

1.5. CME structural components and their motion

To identify the CME structural components and measure their expansion, we examine white-light images obtained by STEREO-A/COR1 and SOHO/LASCO-C2. Figure 9 displays six enhanced-contrast images captured by STEREO-A/COR1. Recall that in the previous section the bright core of the CME was identified with the eruptive prominence. Figure 9, *d–f* shows twisting of the eastern part of the core moving increasingly away from its main body.

Starting at 03:10:50 in Figure 9, *a–d*, a faint halo appears which expands ahead of the CME core until it leaves the COR1 field of view. This halo is the outermost part of the CME, its frontal structure. The average brightness of the small region of the frontal structure visible at 03:15:50 is almost 60 times lower than the brightness of the core that reached the same location at

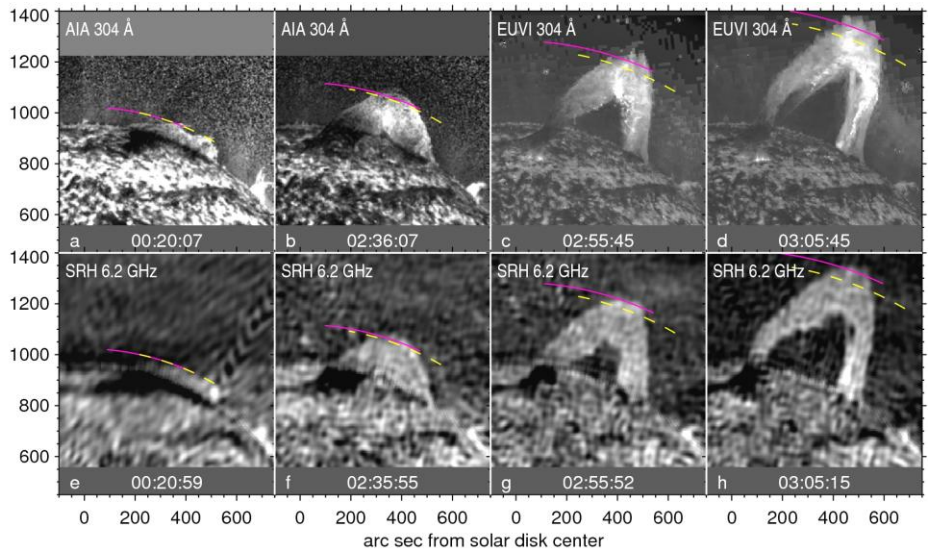

Figure 7. Comparison of images of the eruptive prominence observed in the 304 Å channel by SDO/AIA (*a*, *b*) and STEREO-A/EUVI (*c, d*) with temporally close images obtained by SRH (*e–h*). In all images, the radial brightness distribution was partly subtracted. The yellow dashed arc outlines the middle of the prominence top; the solid magenta arc, the forward-stretching left part

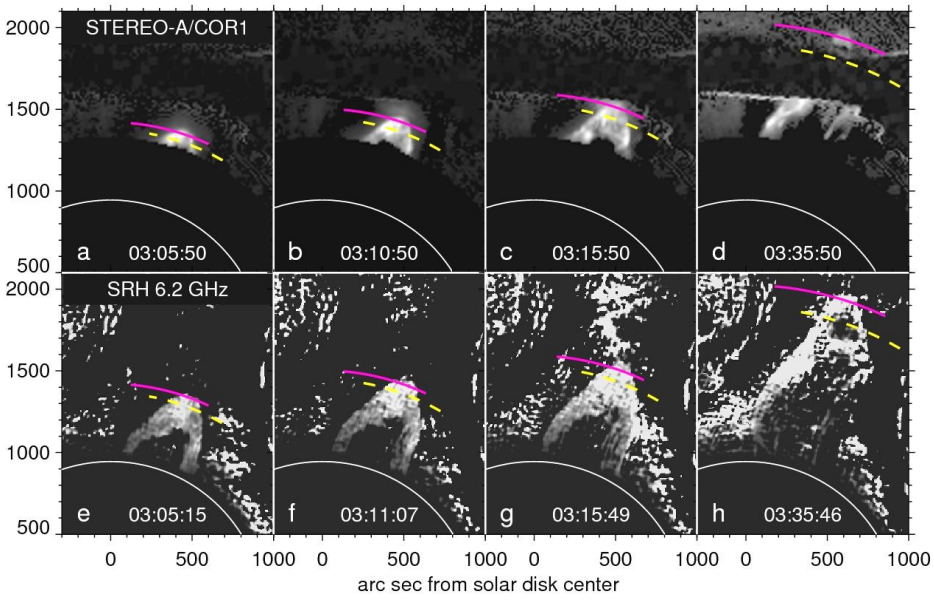

Figure 8. Eruptive prominence in the images obtained: top row — by STEREO-A/COR1 (the 03:00:50 image was subtracted before the CME appearence); bottom row — by SRH (radial distribution of radio brightness was subtracted). The yellow dashed arc outlines the middle part of the prominence top; the magenta arc, the stretching eastern part. The white arc is the solar limb

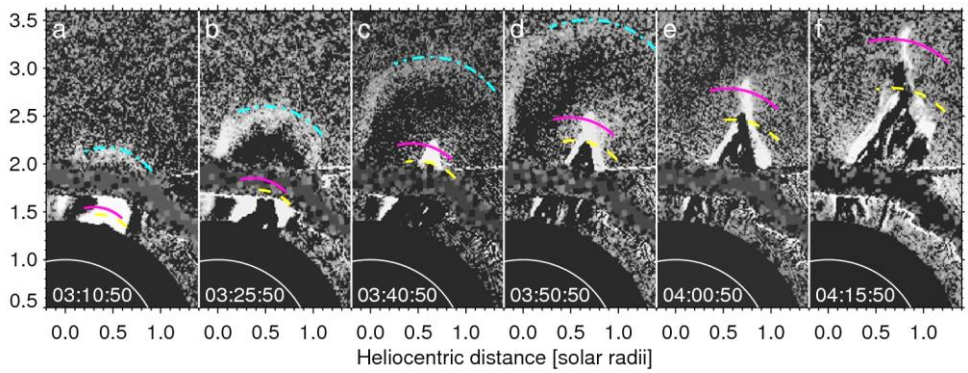

Figure 9. CME structural components in STEREO-A/COR1 images (the 03:00:50 image before the CME appearance was subtracted from each image). The yellow dashed arc delineates the prominence top; the magenta arc, its stretching nose; and the cyan dash-dotted arc, the CME front. The white arc is the solar limb

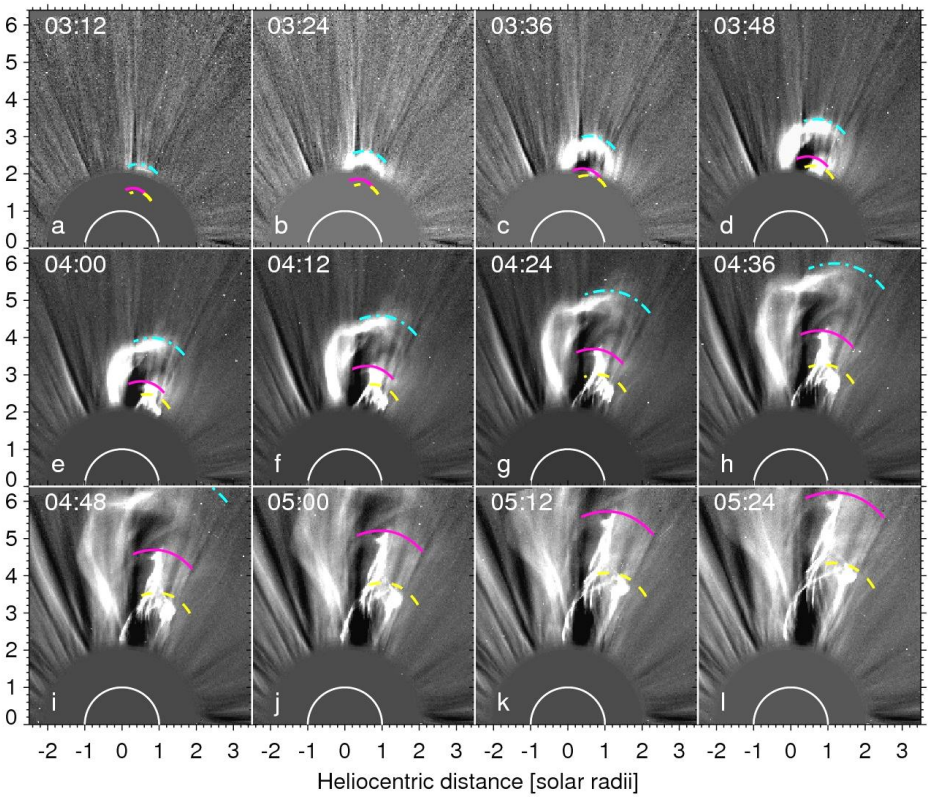

Figure 10. CME structural components in SOHO/LASCO-C2 images, divided by the background image observed before the CME appeared. The designations are the same as in Figure 9

03:45:50. The cyan dash-dotted arc outlines the leading edge of the frontal structure. No manifestations of the frontal structure were detected in either SDO/AIA or STEREO-A/EUVI images in the 193 (195) and 304 Å channels.

The subsequent expansion of the CME is shown in Figure 10. The appearance and position of the CME structural components according to SOHO/LASCO-C2 (see Figure 10) correspond, as a whole, to STEREO-A/COR1 observations (see Figure 9) at close moments in time, with differences determined by the quality and presentation of the images. The twisting of the protruding tip of the core is accompanied by a twisting of lateral parts of the frontal structure, which looks like a multitude of loops. Further expansion of the CME in the SOHO/LASCO-C3 field of view occurred at a nearly constant speed, slightly decelerating (–4 m/s^2). Its study is beyond the scope of this work.

The arcs outlining the eruptive prominence and then the CME structural components in all the examined images obtained with various instruments fit the overall kinematic plots presented in Figure 11. The frontal structure was not detected until 03:10:50, so the initial parts of its kinematic plots had to be completed, assuming a kind of self-similarity in CME expansion. This self-similarity was observed later, when the frontal structure became visible. Its estimated initial height is $0.5R_\odot$, but this height is beyond the SDO/AIA field of view. The frontal structure could be observed with STEREO-A/EUVI, but the EUVI sensitivity near the edge of its field of view is reduced. The lateral parts of the frontal structure were not detected in EUV either.

In all cases, the correspondence of the arcs to the leading edges of the measured objects appears to be quite acceptable, if not perfect. Since different images are presented variously, the leading edges of these objects may be visible at slightly higher or lower altitudes (e.g., parts of the CME core in Figure 9, *e–f* and the corresponding images in Figure 10, *e–f*). The estimated error in timing the second acceleration pulse at 04:07 is several minutes; and in its magnitude and duration (43 min at half-level), within ±15 %. Despite all the uncertainties, the second acceleration is clearly linked to the twisting of the eruptive structure, occurred at ~$2R_\odot$ altitudes, and is comparable in magnitude and duration to the preceding main acceleration pulse.

In Figure 11, *a*, symbols represent measurements in the online CME catalog [http://cdaw.gsfc.nasa.gov/CME_list/] [Yashiro, et al., 2004], carried out for the fastest feature of CME. As shown in Figure 6, this feature was slightly further than the main front and the cyan dash-dotted arc outlining it. This relationship also corresponds to the position of the symbols relative to the blue dash-dotted curve in Figure 11, *a*, which represents our fit. The overall slope of the symbol sequence (i.e. the speed) is somewhat larger than the slope of the fitting curve. Nevertheless, our results are close to the average estimates in the CME catalog: the established speed of the CME front in Figure 11, *b* is 760 km/s — almost the same as the result of the second-order fit in the CME catalog for the first measured points. Thus, the measurements performed in our study provide a detailed picture of CME evolution and are consistent with the estimates in the CME catalog.

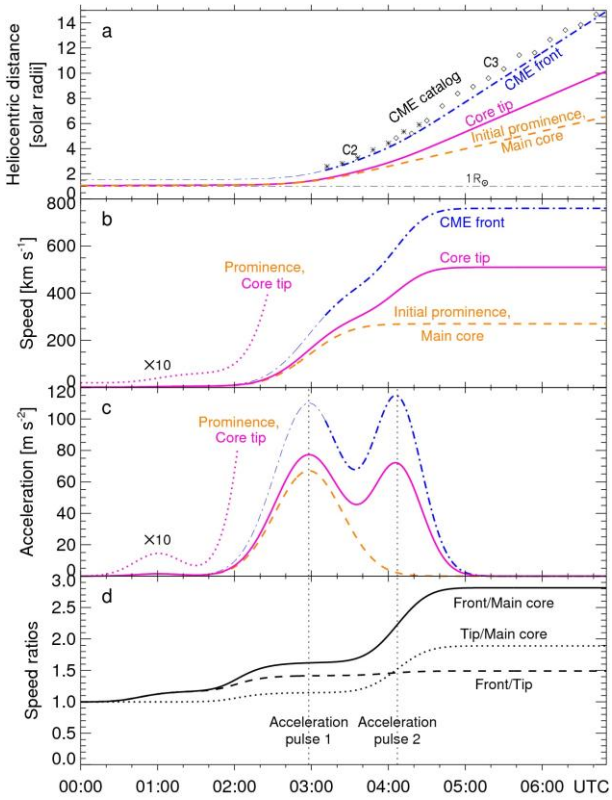

Figure 11. Kinematic characteristics of the eruptive prominence and CME structural components (all measurements relate to their leading edges): the orange dashed line represents the main CME core (eruptive prominence); the solid magenta line, the CME core tip; the blue dash-dotted line, the CME front; thin lines show the initial parts of the plots for which there were no observations. Panel *a* — heliocentric distances. Symbols indicate measurements in the CME catalog: from LASCO-C2 data (asterisks), LASCO-C3 data (diamonds). The gray dash-dotted line denotes the solar limb. In panels *b*, *c*, and *d* are speed plots, acceleration and speed ratios between the CME structural components; the magenta dotted line is the initial part of the plot for the prominence and the core tip magnified by a factor of 10; vertical dotted lines are centroid times of the main acceleration pulses

2. DISCUSSION AND SUMMARY

2.1. Eruptive prominence and CME core

The steady rise of the prominence, with its shape remaining mainly the same until the maximum of the first acceleration at ≈03:00 (see Figures 3, 7), suggests that the torus instability governed the onset of the eruption. A similar conclusion was drawn in [Filippov, 2024] from analysis of a number of eruptions. At ~$2R_\odot$ altitudes, the eastern part of the prominence — the CME core — started to noticeably stretch forward and twist (see Figures 9, 10), which corresponds to the second acceleration with a maximum at 04:07. This phenomenon clearly demonstrates the development of helical kink instability, which did not affect the expansion of the main core. A similar transformation of eruptive prominences has been observed before (see, e.g., [Aschwanden et al., 2009, Figure 14; Grechnev et al., 2018, Figure 13]).

Note that the apparent complexity of the shape of the eruptive prominence and the CME core may be due to the peculiarities of its three-dimensional configuration (e.g., [Koutchmy et al., 2008]). As known, due to gravity, the bulk of the mass of a quiescent prominence is concentrated in the lowest locations, where magnetic field lines are concave (see, e.g., [Gibson, 2018]). This location corresponds to the lower part of the invisible volumetric magnetic flux rope that is the magnetic skeleton of the seemingly thin prominence. From above, the prominence appears as a filament consisting of numerous threads located nearly along the inversion line of the radial magnetic field. From the side, the prominence looks like a band-like mesh of these threads extended along the magnetic field lines. Helical kink instability of the invisible volumetric magnetic flux rope is observed as a helical bend of this visible mesh. The development and stretch of the helical bend upward in the final nonlinear stage creates a visual impression of a tip growing out from the prominence body (see Figures 9, *e–f* and 10, *g–l*). The pattern observed in this event resembles the scheme of the helical bend in Figure 2, *a* in [Uralov, 1990a].

The proposed interpretation of the visual manifestation of the helical bend of the magnetic flux rope is a simplification. In a real eruption, the accelerated expansion and change in the shape of the magnetic flux rope are accompanied by a redistribution of the prominence mass (see, e.g., [Filippov, Koutchmy, 2002]). In our case of relatively low eruptive accelerations of the prominence (≤0.25$g_\odot$, where $g_\odot$ is the solar gravity acceleration), the clearly visible effect of its draining, i.e. ejected plasma flows back to the solar surface, proves to be significant.

2.2. Frontal structure

In this event, the frontal structure was observed only by coronagraphs. The brightness of the structures visible in white light due to Thomson scattering is proportional to the free electron density. The brightness of the optically thin structures emitting EUV emission lines and thermal radio bremsstrahlung is proportional to the emission measure, i.e. the square of the emitting particle density. According to the estimate in Subsection 1.5, the brightness of the frontal structure in the STEREO/COR1 image was lower by a factor of almost 60 than the brightness of the core observed at the same location half an hour later. With such a brightness ratio, it is difficult to detect the frontal structure even in images obtained by EUV telescopes with focusing optics. The dynamic range of Fourier-synthesis interferometers is much narrower, so the frontal structure is unlikely to be detected in the microwave range.

According to the SOHO/LASCO-C2 images (Figure 10), the frontal structure consisted of multiple loops. Before the eruption, the prominence should have been surrounded by a coronal arcade, so the frontal structure was most likely formed from this arcade. Magnetic fields in such arcades are close to potential ones; therefore, the frontal structure could hardly be active. It is more likely that its expansion was caused by the expansion of an active

magnetic flux rope within it. Accordingly, visible changes in the frontal structure reflected changes occurring in CME's internal structure.

There should be a separatrix surface between the magnetic domain, which contained closed structures of the prominence and arcades above it before the eruption, and the outer coronal structures open to interplanetary space. The rise of the erupting structures causes the separatrix surface to expand, preventing plasma penetration through it and acting as an isotropic piston. As a result, the plasma is forced out of the volume it previously occupied, forming a compressed layer ahead of the CME. This plasma pileup could be the reason for the considerable excess of the CME mass over the mass of the eruptive prominence estimated in [Koutchmy et al., 2008]. Presumably, the compressed plasma layer in front of a CME is present until the surrounding plasma begins to flow around the CME.

2.3. Helical kink instability and kinematic relationships between CME structural components

Our kinematic analysis has revealed two main acceleration pulses of the CME (see Figures 5, 11). The first, main acceleration pulse corresponds to the kinematic similarity between all three spatially separated CME structures outlined by yellow, magenta, and cyan arcs in Figures 6–10. Initially, the expansion was self-similar — the shape and relative positions of different components of its structure remained unchanged. During the second pulse, this similarity was disrupted. After the second acceleration pulse, the self-similar expansion of all three structural components of the CME was resumed.

An indicator of the self-similar expansion of the CME structural components, conventionally designated by the indices i=1 and i=2, is the equality and constancy of the ratios of velocities v_i, accelerations a_i, and distances r_i of elements, which correspond to each other, to some, a priori unknown expansion center: $v_1/v_2=a_1/a_2=r_1/r_2=k$, where k is a constant value [Uralov et al., 2005]. To assess self-similarity, it therefore suffices to know the behavior of the v_1/v_2 ratio. This ratio for different pairs of CME components is shown in Figure 11, *d*. The horizontal regions correspond to the consistent self-similar expansion of the selected elements. All three lines were horizontal within the interval of the first acceleration pulse (the maximum of the pulse at ≈03:00 is indicated by the dotted line). The interval of the second acceleration pulse (the pulse maximum is indicated by the dotted line at ≈04:00) corresponds to the continuation of only one horizontal line Front/Tip. During this period, there was no synchronization between the main core and front or between the main core and tip. After the second pulse (after 04:30), synchronization was resumed — all three lines in Figure 11, *d* became horizontal and parallel again.

During the first acceleration pulse, a coordinated expansion of the frontal structure and the prominence, which retained its toroidal shape, occurred. This pulse was caused by torus instability. The second acceleration pulse was produced by helical kink instability, whose development can be seen in the helical deformation of the shape and size of the eruptive prominence in Figures 9, 10 and in violation of the kinematic self-similarity of the CME in Figure 11, *d*. The subsequent virtually inertial expansion of the newly shaped prominence became self-similar again.

Further confirmation that we are indeed dealing with helical kink instability can be provided by a qualitative assessment of the spatial size of the helical disturbance at the nonlinear stage. The instability is caused by the external helical magnetic field surrounding the magnetic flux rope; it is this field that "breaks" the magnetic flux rope. The helical bending of the flux rope is accompanied by an increase in its length and straightening of external magnetic field lines. Let us use the frozen-in condition of the magnetic field in the form of the equality of two magnetic fluxes: a) the poloidal magnetic flux between the conventional boundary of the unperturbed magnetic flux rope and the separatrix surface of the magnetic domain within which this flux rope is located; b) the magnetic flux that envelops the magnetic flux rope after the helical kink instability ceases. For characteristic radii of the flux rope b and the separatrix surface d, the typical radius of the helical bend $R_{\text{kink}} \approx b\sqrt{2\ln\frac{d}{b}}$. This relation is given in [Kadomtsev, 1966, § 9] to estimate the radius of the equilibrium spiral for the helical kink instability of electric current in a plasma cylinder of radius b surrounded by a perfectly conducting sheath of radius d. In our case, the sheath is represented by the separatrix surface. The radius b of the magnetic flux rope is unknown, but it is not less than the apparent width of the eruptive prominence. Assuming that for a thick magnetic flux rope $R_{\text{kink}}\approx b$, we have $2\ln\frac{d}{b}\approx 1$, and then $R_{\text{kink}} \approx d/\sqrt{e} = 0.6d$. The separatrix surface of the magnetic domain in which the eruption occurred determines the size of the coronal magnetic cavity of the CME, as well as the location of the frontal structure. The size of the additional CME "swelling" caused by helical kink instability is therefore comparable to the size of the frontal structure, as in the event under discussion.

The above reasonings do not take into account the possible presence of reverse electric currents that shield the forward current within the magnetic flux rope. The presence of reverse currents alters equilibrium conditions of the magnetic flux rope (e.g. [Solovev, Uralov, 1979]) and reduces the effectiveness of helical kink instability (e.g., [Uralov, 1990b; Tsap et al., 2020]). In this regard, it is worth noting that the effects of shielding of magnetic structures by reverse currents are more important at the moments when new magnetic fluxes emerge from beneath the photosphere into the corona and are insignificant later on.

RESULTS AND CONCLUSIONS

The eruption of a high-latitude prominence on June 12 2023 was observed by SRH out to heliocentric distances exceeding two solar radii with sufficient temporal resolu-

tion to identify features of its development and changes in its shape. Detailed SRH observations over a wide altitude range confirmed the correctness of transformations of all the examined images, obtained by various instruments, and ensured a reliable identification of the CME structural components visible in different emission ranges.

The eruptive event led to the development of a CME. The eruptive prominence became the CME core, while the arcade that previously surrounded it formed the frontal structure. Its probable initial height above the solar surface is estimated at $0.5R_{\odot}$. The frontal structure and the pre-eruptive arcade that formed it were not detected in EUV in this event, and they are unlikely to be found in microwave images in this or other events.

Two acceleration pulses comparable in magnitude and duration have been revealed in the expansion of the eruptive prominence that became the CME core. Apparently, the first acceleration was caused by the development of torus instability in the magnetic flux rope, whose visible part was the prominence; and the second, by its helical kink instability. The development of helical kink instability manifested in the stretching and twisting of the eruptive prominence top did not affect the expansion of its massive lower portion, but influenced the motion and shape of the CME frontal structure. The CME expansion was self-similar both during the torus instability and during the final stage of unlimited inertial expansion of all CME structural components. During the intermediate stage of helical kink instability, only kinematic similarity between the frontal structure and the top of the growing helical bend was retained. The involvement of helical kink instability in initiating torus instability is ruled out by the fact of its much later switch-on, which is consistent with the conclusions drawn in [Filippov, 2024].

We are grateful to our colleagues from the Radio Astrophysical Department and the Radio Astrophysical Observatory in Badary, as well as to S.V. Lesovoi, A.A. Kochanov, and V.I. Kiselev for their assistance in handling the SRH data. We thank the reviewers for their helpful comments. We are indebted to the NASA/SDO and AIA research teams, the STEREO/SECCHI research and instrument teams at NASA, and the SOHO/LASCO team. SOHO is a project of international cooperation between ESA and NASA. We are grateful to the team that generates and maintains the CME catalog at the CDAW Data Center by NASA and The Catholic University of America in cooperation with the Naval Research Laboratory.

The work was financially supported by the Ministry of Science and Higher Education of the Russian Federation. The results were obtained using the Large-Scale Research Facility "Radioheliograph" of ISTP SB RAS [https://ckp-rf.ru/catalog/usu/4138190/].

REFERENCES

Alissandrakis C.E., Kochanov A.A., Patsourakos S., et al. Microwave and EUV observations of an erupting filament and associated flare and coronal mass ejections. *Publ. Astron. Soc. Japan*. 2013, vol. 65, iss. SP1, S8. https://doi.org/10.1093/pasj/65.sp1.S8.

Altyntsev A.T., Lesovoi S.V., Globa M.V., et al. Multiwave Siberian Radioheliograph. *Sol-Terr. Phys.* 2020, vol. 6, iss. 2, pp. 30–40. https://doi.org/10.12737/stp-62202003.

Amari T., Luciani J.F. Confined disruption of a three-dimensional twisted magnetic flux tube. *Astrophys. J.* 1999, vol. 515, iss. 2, pp. L81–L84. https://doi.org/10.1086/311971.

Amari T., Luciani J.F., Mikic Z., Linker J.A. Twisted flux rope model for coronal mass ejections and two-ribbon flares. *Astrophys. J. Lett*. 2000, vol. 529, iss. 1, pp. L49–L52. https://doi.org/10.1086/312444.

Amari T., Canou A., Aly J.-J. Characterizing and predicting the magnetic environment leading to solar eruptions. *Nature*. 2014, vol. 514, iss. 7523, pp. 465–469. https://doi.org/10.1038/nature13815.

Aschwanden M.J., Wuelser J.P., Nitta N.V., Lemen J.R. Solar flare and CME observations with STEREO/EUVI. *Solar Phys*. 2009, vol. 256, iss. 1-2, pp. 3–40. https://doi.org/10.1007/s11207-009-9347-4.

Aulanier G., Török T., Démoulin P., DeLuca E.E. Formation of torus-unstable flux ropes and electric currents in erupting sigmoids. *Astrophys. J.* 2010, vol. 708, iss. 1, pp. 314–333. https://doi.org/10.1088/0004-637X/708/1/314.

Bateman G. *MHD Instabilities*. Cambridge, MA, MIT Press, 1978, 270 p.

Bein B.M., Berkebile-Stoiser S., Veronig A.M., et al. Impulsive acceleration of coronal mass ejections. I. Statistics and coronal mass ejection source region characteristics. *Astrophys. J.* 2011, vol. 738, 191. https://doi.org/10.1088/0004-637X/738/2/191.

Bellan P.M. *Fundamentals of Plasma Physics*. Cambridge, UK, Cambridge University Press, 2008, 628 p.

Berkebile-Stoiser S., Veronig A.M., Bein B.M., Temmer M. Relation between the coronal mass ejection acceleration and the non-thermal flare characteristics. *Astrophys. J.* 2012, vol. 753, 88. https://doi.org/10.1088/0004-637X/753/1/88.

Borovik V.N. Quiet Sun from multifrequency radio observations on RATAN-600. *Adv. Solar Phys.* 1994, vol. 432, pp. 185–190. https://doi.org/10.1007/3-540-58041-7_217.

Brueckner G.E., Howard R.A., Koomen M.J., et al. The Large Angle Spectroscopic Coronagraph (LASCO). *Solar Phys.* 1995, vol. 162, pp. 357–402. https://doi.org/10.1007/BF00733434.

Bruno A., Bazilevskaya G.A., Boezio M., et al. Solar energetic particle events observed by the PAMELA mission. *Astrophys. J.* 2018, vol. 862, iss. 2, 97. https://doi.org/10.3847/1538-4357/aacc26.

Chen J. Effects of toroidal forces in current loops embedded in a background plasma. *Astrophys. J.* 1989, vol. 338, pp. 453–470. https://doi.org/10.1086/167211.

Domingo V., Fleck B., Poland A.I. The SOHO Mission: An Overview. *Solar Phys.* 1995, vol. 162, pp. 1–37. https://doi.org/10.1007/BF00733425.

Filippov B. Development of torus and kink instabilities in eruptive prominences. *Astrophys. J.* 2024, vol. 977, iss. 2, 259. https://doi.org/10.3847/1538-4357/ad95fe.

Filippov B., Koutchmy S. About the prominence heating mechanisms during its eruptive phase. *Solar Phys.* 2002, vol. 208, iss. 2, pp. 283–295. https://doi.org/10.1023/A:1020532607451.

Gallagher P.T., Lawrence G.R., Dennis B.R. Rapid acceleration of a coronal mass ejection in the low corona and implications for propagation. *Astrophys. J. Lett.* 2003, vol. 588, pp. L53–L56. https://doi.org/10.1086/375504.

Gibson S.E. Solar prominences: theory and models. Fleshing out the magnetic skeleton. *Living Rev. Solar Phys*. 2018, vol. 15, iss. 1, 7. https://doi.org/10.1007/s41116-018-0016-2.

Gopalswamy N., Hanaoka Y. Coronal dimming associated with a giant prominence eruption. *Astrophys. J.* 1998, vol. 498, iss. 2, pp. L179–L182. https://doi.org/10.1086/311330.

Grechnev V.V., Kuzmenko I.V. A geoeffective CME caused by the eruption of a quiescent prominence on 29 September 2013. *Solar Phys.* 2020, vol. 295, 55. https://doi.org/10.1007/s11207-020-01619-x.

Grechnev V.V., Uralov A.M., Zandanov V.G., Baranov N.Y., Shibasaki K. Observations of prominence eruptions with two radioheliographs, SSRT, and NoRH. *Pub. Astron. Soc. Japan.* 2006, vol. 58, no. 1, pp. 69–84. https://doi.org/10.1093/pasj/58.1.69.

Grechnev V.V., Uralov A.M., Kochanov A.A., et al. A tiny eruptive filament as a flux-rope progenitor and driver of a large-scale CME and wave. *Solar Phys.* 2016, vol. 291, pp. 1173–1208. https://doi.org/10.1007/s11207-016-0888-z.

Grechnev V.V., Lesovoi S.V., Kochanov A.A., et al. Multi-instrument view on solar eruptive events observed with the Siberian Radioheliograph: From detection of small jets up to development of a shock wave and CME. *J. Atmos. Solar-Terr. Phys.* 2018, vol. 174, pp. 46–65. https://doi.org/10.1016/j.jastp.2018.04.014.

Grechnev V.V., Kiselev V.I., Uralov A.M., Myshyakov I.I. Reconciling observational challenges to the impulsive-piston shock-excitation scenario. II. Shock waves produced in CME-less events with a null-point topology. *Solar Phys.* 2022, vol. 297, 123. https://doi.org/10.1007/s11207-022-02061-x.

Grechnev V.V., Kiselev V.I., Uralov A.M., et al. Mysteries of the 17 May 2012 solar event responsible for GLE71. I. CME development and the role of disturbances excited by eruptions. *Solar Phys.* 2024, vol. 299, 129. https://doi.org/10.1007/s11207-024-02373-0.

Hanaoka Y., Shibasaki K., Nishio M., et al. Processing of the Nobeyama Radioheliograph data. *Proc. of Kofu Symposium*. Kofu, Japan, 1994, pp. 35–43.

Hassanin A., Kliem B. Helical kink instability in a confined solar eruption. *Astrophys. J.* 2016, vol. 832, iss. 2, 106. https://doi.org/10.3847/0004-637X/832/2/106.

Hassanin A., Kliem B., Seehafer N., Török T. A model of homologous confined and ejective eruptions involving kink instability and flux cancellation. *Astrophys. J. Lett.* 2022, vol. 929, iss. 2, L23. https://doi.org/10.3847/2041-8213/ac64a9.

Howard R.A., Moses J.D., Vourlidas A., et al. Sun Earth Connection Coronal and Heliospheric Investigation (SECCHI). *Space Sci. Rev.* 2008, vol. 136, pp. 67–115. https://doi.org/10.1007/s11214-008-9341-4.

Kadomtsev B.B. Hydromagnetic stability of a plasma. *Reviews of Plasma Physics*. Consultants Bureau, New York, 1966, vol. 2, p. 153.

Kaiser M.L., Kucera T.A., Davila J.M., et al. The STEREO Mission: An introduction. *Space Sci. Rev.* 2008, vol. 136, pp. 5–16. https://doi.org/10.1007/s11214-007-9277-0.

Kliem B., Török T. Torus Instability. *Phys. Rev. Lett.* 2006, vol. 96, iss. 25, 255002. https://doi.org/10.1103/PhysRevLett.96.255002.

Kochanov A.A., Anfinogentov S.A., Prosovetsky D.V., et al. Imaging of the solar atmosphere by the Siberian Solar Radio Telescope at 5.7 GHz with an enhanced dynamic range. *Publ. Astron. Soc. Japan.* 2013, vol. 65, no. SP1, S19. https://doi.org/10.1093/pasj/65.sp1.S19.

Koutchmy S., Slemzin V., Filippov B., et al. Analysis and interpretation of a fast limb CME with eruptive prominence, C-flare, and EUV dimming. *Astron. Astrophys.* 2008, vol. 483, iss. 2, pp. 599–608. https://doi.org/10.1051/0004-6361:20078311.

Kuzmenko I.V., Grechnev V.V. Development and parameters of a non-self-similar CME caused by the eruption of a quiescent prominence. *Solar Phys.* 2017, vol. 292, iss. 10, article id. 143. https://doi.org/10.1007/s11207-017-1167-3.

Lemen J.R., Title A.M., Akin D.J., et al. The Atmospheric Imaging Assembly (AIA) on the Solar Dynamics Observatory (SDO). *Solar Phys.* 2012, vol. 275, pp. 17–40. https://doi.org/10.1007/s11207-011-9776-8.

Ma S., Raymond J.C., Golub L., et al. Observations and interpretation of a low coronal shock wave observed in the EUV by the SDO/AIA. *Astrophys. J.* 2011, vol. 738, 160. https://doi.org/10.1088/0004-637X/738/2/160.

Molodenskii M.M., Filippov B.P. Rapid motion of filaments in solar active regions — Part two. *Sov. Astron.* 1987, vol. 31, iss. 5, pp. 564–568.

Moore R.L., Sterling A.C., Hudson H.S., Lemen J.R. Onset of the magnetic explosion in solar flares and coronal mass ejections. *Astrophys. J.* 2001, vol. 552, iss. 2, pp. 833–848. https://doi.org/10.1086/320559.

Pesnell W.D., Thompson B.J., Chamberlin P.C. The Solar Dynamics Observatory (SDO). *Solar Phys*. 2012, vol. 275, pp. 3–15. https://doi.org/10.1007/s11207-011-9841-3.

Schmieder B., Démoulin P., Aulanier G. Solar filament eruptions and their physical role in triggering coronal mass ejections. *Adv. Space Res.* 2013, vol. 51, iss. 11, pp. 1967–1980. https://doi.org/10.1016/j.asr.2012.12.026.

Shafranov V.D. Plasma equilibrium in a magnetic field. *Reviews of Plasma Physics*. Vol. 2. New York, Consultants Bureau, 1966, p. 103.

Shafranov V.D. To the question of hydromagnetic stability of a plasma column with current in a strong magnetic field. *Technical Physics.* 1970, vol. 40, no. 2, pp. 241–253. (In Russian).

Sheeley N.R., Jr., Warren H.P., Wang Y.-M. A streamer ejection with reconnection close to the Sun. *Astrophys. J.* 2007, vol. 671, pp. 926–935. https://doi.org/10.1086/522940.

Shimojo M., Yokoyama T., Asai A., et al. One solar-cycle observations of prominence activities using the Nobeyama Radioheliograph 1992–2004. *Publ. Astron. Soc. Japan*. 2006, vol. 58, no. 1, pp. 85–92. https://doi.org/10.1093/pasj/58.1.85.

Solovev A.A., Uralov A.M. Equilibrium and stability of magnetic flux ropes on the Sun. *Soviet Astron. Lett.* 1979, vol. 5, pp. 250–252.

Švestka Z. Varieties of coronal mass ejections and their relation to flares. *Space Sci. Rev.* 2001, vol. 95, iss. 1/2, pp. 135–146. https://doi.org/10.1023/A:1005225208925.

Temmer M., Veronig A.M., Kontar E.P., et al. Combined STEREO/RHESSI study of coronal mass ejection acceleration and particle acceleration in solar flares. *Astrophys. J.* 2010, vol. 712, pp. 1410–1420. https://doi.org/10.1088/0004-637X/712/2/1410.

Van Tend W., Kuperus M. The development of coronal electric current systems in active regions and their relation to filaments and flares. *Solar Phys.* 1978, vol. 59, iss. 1, pp. 115–127. https://doi.org/10.1007/BF00154935.

Tsap Y., Fedun V., Cheremnykh O., et al. On the stabilization of a twisted magnetic flux tube. *Astrophys. J.* 2020, vol. 901, iss. 2, 99. https://doi.org/10.3847/1538-4357/abaf01.

Uralov A.M. The flare as a result of cross-interaction of loops: Causal relationship with a prominence. *Solar Phys.* 1990a, vol. 127, iss. 2, pp. 253–265. https://doi.org/10.1007/BF00152165.

Uralov A.M. External helical modes of a solitary current in an unconfined plasma. *Radiophysics and Quantum Electronics*. 1990b. vol. 33, iss. 10, pp. 859–865.

Uralov A.M., Grechnev V.V., Hudson H.S. Initial localization and kinematic characteristics of the structural components of a coronal mass ejection. *J. Geophys. Res.: Space Phys.* 2005, vol. 110, iss. A5, A05104. https://doi.org/10.1029/2004JA010951.

Uralov A.M., Grechnev V.V., Lesovoi S.V., Globa M.V. Plasma heating in an erupting prominence detected from microwave observations with the Siberian Radioheliograph. *Solar Phys*. 2023, vol. 298, iss. 10, 117. https://doi.org/10.1007/s11207-023-02210-w.

Vršnak B., Maričić D., Stanger A.L., et al. Acceleration phase of coronal mass ejections: I. Temporal and spatial scales. *Solar Phys.* 2007, vol. 241, pp. 85–98. https://doi.org/10.1007/s11207-006-0290-3.

Wang Y., Zhang J., Shen C. An analytical model probing the internal state of coronal mass ejections based on observations of their expansions and propagations. *J. Geophys. Res.* 2009, vol. 114, A10104. https://doi.org/10.1029/2009JA014360.

Wuelser J.-P., Lemen J.R., Tarbell T.D., et al. EUVI: the STEREO-SECCHI Extreme Ultraviolet Imager. *Telescopes and Instrumentation for Solar Astrophysics. SPIE Conf. Ser.* 2004, vol. 5171, pp. 111–122. https://doi.org/10.1117/12.506877.

Yashiro S., Gopalswamy N., Michalek G., et al. A catalog of white light coronal mass ejections observed by the SOHO spacecraft. *J. Geophys. Res.: Space Phys.* 2004, vol. 109, A07105. https://doi.org/10.1029/2003JA010282.

Zheleznyakov V.V. *Radio Emission of the Sun and Planets*. Oxford, Pergamon Press, 1970, 701 p. https://doi.org/10.1016/C2013-0-02176-7.

Zirin H., Baumert B.M., Hurford G.J. The microwave brightness temperature spectrum of the quiet Sun. *Astrophys. J.* 1991, vol. 370, pp. 779–783. https://doi.org/10.1086/169861.

URL: http://cdaw.gsfc.nasa.gov/CME_list/ (accessed December 20, 2025).

URL: https://ckp-rf.ru/catalog/usu/4138190/ (accessed December 20, 2025).

Original Russian version: Grechnev V.V., Globa M.V., Uralov A.M., published in Solnechno-zemnaya fizika. 2026, vol. 12, no. 2, pp. 10–23. https://doi.org/10.12737/szf-122202602.

How to cite this article

Grechnev V.V., Globa M.V., Uralov A.M. Eruption of a high-latitude prominence observed by the Siberian Radioheliograph and space-borne telescopes: I. Torus and helical kink instabilities in CME development. *Sol.-Terr. Phys*. 2026, vol. 12, iss. 2, pp. 8–20. https://doi.org/10.12737/stp-122202602.